SDR FRAMEWORK FOR BURST/ CONTINUOUS MPSK/ 16-QAM MODEMS

S. Jayasimha, P. Jyothendar and S. Pavanalatha

Signion Systems Ltd.
20, Rockdale Compound
Somajiguda, Hyderabad-500082
info@signion.com

ABSTRACT

We describe a software-defined radio (SDR) framework for MPSK/16-QAM pulse-shaping, demodulation, carrier acquisition and tracking for satellite modems. Analytical performance bounds for burst and continuous mode acquisition are validated with measured performance.

1. INTRODUCTION

As satellite launch costs decline, both power (E_b/N_0) and bandwidth efficiency (bps/Hz) determine a transponder's economic value (rather than simply the former). Power efficiency is achieved with lower order modulations (such as BPSK and QPSK), while spectral efficiency is achieved using higher order modulations (HOMs), typically 8-PSK and 16-QAM. Amongst HOMs, constant envelope modulation (CEM) minimizes spectral re-growth associated with high efficiency (e.g., class-C) amplification. For burst-mode multiple-access, reduced preambles (for frequency offset and symbol-timing acquisition) enhance throughput. A satellite transceiver (Figure 1) is generally realized using a configurable software radio [1] with reusable kernels for:

- reduced ISI and spectral re-growth pulse-shaping for all modulations, including HOMs
- burst and continuous mode carrier acquisition
- demodulator algorithms
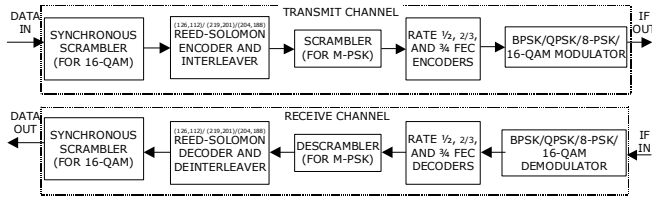
Figure 1. BPSK, QPSK, 8-PSK and 16-QAM transceiver

In a similar vein, coding standards for 8-PSK and 16-QAM (e.g., for satcom) use pragmatic trellis (PTCM) and outer codes that rely on two "industry standard" kernels: a constraint length 7, rate ½, inner code and Reed-Solomon outer coding over $GF(2^8)$. Figure 2 shows 8-PSK and 16-QAM PTCM [2] encoders respectively.
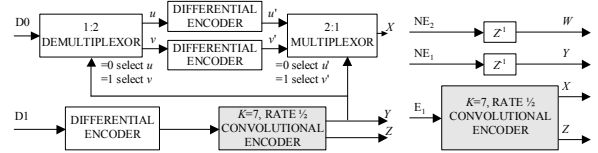
Figure 2. Reusable modules (shaded) in ambiguity-encoded 8-PSK and $n \cdot \pi/2$-variant 16-QAM PTCM

2. PULSE-SHAPING

Feher [3] *n*-sample pulse-shapes are extendable to longer window-lengths [4] and HOMs, e.g., for *n*=2, samples for the *k*th 8-PSK or 16-QAM symbol, with bits $[X_k Y_k Z_k]$ or $[W_k X_k Y_k Z_k]$ respectively, are obtained by indexing Table 1 using 4-bit patterns, $[(X_k \oplus Y_k)Z_k (X_{k+1} \oplus Y_{k+1})Z_{k+1}]$ or $[W_k (W_k \oplus Z_k)W_{k+1}(W_{k+1} \oplus Z_{k+1})]$, for in-phase (*I*), $[X_k \overline{Z}_k X_{k+1} \overline{Z}_{k+1}]$ or $[X_k (X_k \oplus Y_k)X_{k+1}(X_{k+1} \oplus Y_{k+1})]$, for quadrature (*Q*) channels, derived from a 2-symbol input data window $[X_k Y_k Z_k X_{k+1} Y_{k+1} Z_{k+1}]$ or $[W_k X_k Y_k Z_k W_{k+1} X_{k+1} Y_{k+1} Z_{k+1}]$ (Appendix 1 derives the 8-PSK and 16-QAM PSD for any given pulse-shape set).

I : $X_k \oplus Y_k$	Z_k	$X_{k+1} \oplus Y_{k+1}$	Z_{k+1}	
I_{QAM} : W_k	$W_k \oplus Z_k$	W_{k+1}	$W_{k+1} \oplus Z_{k+1}$	2-sample waveform
Q : X_k	$\overline{Z}_k$	X_{k+1}	$\overline{Z}_{k+1}$	
Q_{QAM}: X_k	$X_k \oplus Y_k$	X_{k+1}	$X_{k+1} \oplus Y_{k+1}$	
0	0	0	0	*a, a*
0	0	0	1	*z, y*
0	0	1	0	*z, -z*
0	0	1	1	*z, -x*
0	1	0	0	*y, z*
0	1	0	1	*b, b*
0	1	1	0	*x, -z*
0	1	1	1	*x, -x*
1	0	0	0	*-z, z*
1	0	0	1	*-z, x*
1	0	1	0	*-a, -a*
1	0	1	1	*-z, -y*
1	1	0	0	*-x, z*
1	1	0	1	*-x, x*
1	1	1	0	*-y, -z*
1	1	1	1	*-b, -b*

Table 1. 16-QAM/ 8-PSK/ QPSK pulse-shaping waveforms with inverse sinc correction (*a*=1, *b*=0.4142, *x*=0.3292, *y*=0.6193, *z*=0.7949)

For QPSK, 2-input bits I_k and Q_k, generate the 3-bit symbol subset $[X_k Y_k Z_k]$ of Figure 3 ($X_k = \overline{Q_k}$, $Y_k = I_k \oplus Q_k$, $Z_k = Y_k$; with $I_k = Q_k$ for BPSK) that is used identically to obtain the kth symbol's pulse shapes. Thus, a common pulse-shaping ROM is used for MPSK and 16-QAM.
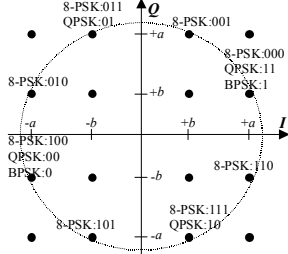
Figure 3. Subset of 16-QAM ($W_k X_k Y_k Z_k$) used for 8-PSK ($X_k Y_k Z_k$), QPSK and BPSK

3. DEMODULATION

Demodulation (Figure 4) comprises efficient I/Q baseband conversion using interpolated FIR (IFIR) decimation filters [5], numerically controlled oscillator (NCO)/ mixer-based frequency-offset tracking, matched filtering and synchronization processing. The latter consists of phase estimation at each baud time offset and using the phase at a selected time offset for coherent demodulation.
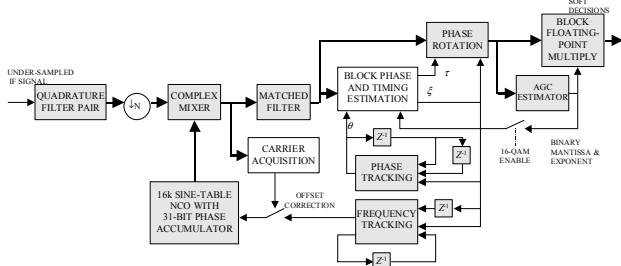
Figure 4. Reusable (shaded blocks) demodulator structure

Phase estimation accuracy, obtained at the demodulator frequency tracking range's expense, is determined by the decision-directed phase-locked loop (DDPLL) bandwidth as described in [6] and [7], assuming that frequency jitter, determined by the NCO's sine table length and its phase accumulator's ultimate (word-size dependent) frequency resolution, is small. For MPSK, the DDPLL forms decision variables on each T_s-second baud's in-phase (R_k) and quadrature (S_k) samples and improves carrier phase estimate over an N-symbol block for each of L equally spaced baud time hypotheses[1], σ. For QPSK and BPSK, the phase estimator's decision variables are:

---

[1]For time offsets, $\sigma=1, \ldots, L$, the symbol synchronized offset selected, σ_m, has the maximum of all block energies $E(\sigma) = R_{sum}^2(\sigma) + S_{sum}^2(\sigma)$. Parallel demodulation of T_s/L-spaced time offsets (rather than sequential timing recovery) allows shortening of burst-mode preamble, usually composed of un-modulated carrier recovery (CR), bit-timing recovery (BTR) and low aperiodic autocorrelation unique word (UW), by omitting BTR.

$$\left.\begin{array}{l} T_{rk}(\sigma) = R_k(\sigma)\cos[\theta(\sigma)] + S_k(\sigma)\sin[\theta(\sigma)] \\ T_{sk}(\sigma) = S_k(\sigma)\cos[\theta(\sigma)] - R_k(\sigma)\sin[\theta(\sigma)] \end{array}\right\}, \sigma = 1,\cdots, L \quad (1)$$

For QPSK, hard decoding of $T_{rk}(\sigma)$ and $T_{sk}(\sigma)$ yields channel bits $I_k(\sigma)$ and $Q_k(\sigma)$, which are processed to estimate phase[2] for each time offset using:

$$\left.\begin{array}{l} R_{sum}(\sigma) = \sum_N I_k(\sigma)T_{rk}(\sigma) + Q_k(\sigma)T_{sk}(\sigma) \\ S_{sum}(\sigma) = \sum_N I_k(\sigma)T_{sk}(\sigma) - Q_k(\sigma)T_{rk}(\sigma) \\ \theta(\sigma) = \tan^{-1}\left[S_{sum}(\sigma)/R_{sum}(\sigma)\right] \end{array}\right\}, \sigma = 1,\cdots, L \quad (2)$$

For BPSK, hard decoding of $T_{rk}(\sigma)+T_{sk}(\sigma)$ is used instead:

$$\left.\begin{array}{l} R_{sum}(\sigma) = \sum_N I_k(\sigma)\left[T_{sk}(\sigma) + T_{rk}(\sigma)\right] \\ S_{sum}(\sigma) = \sum_N I_k(\sigma)\left[T_{sk}(\sigma) - T_{rk}(\sigma)\right] \\ \theta(\sigma) = \tan^{-1}\left[S_{sum}(\sigma)/R_{sum}(\sigma)\right] \end{array}\right\}, \sigma = 1,\cdots, L \quad (3)$$

An additional step of doubling QPSK decision variables' phase allows the QPSK process to be extended for 8-PSK (and, indeed, to any 2^m-order CEMs, $m \geq 4$) as follows:

$$\text{Phase doubling:} \left.\begin{array}{l} T'_{rk}(\sigma) = T_{rk}^2(\sigma) - T_{sk}^2(\sigma) \\ T'_{sk}(\sigma) = 2 \cdot T_{rk}(\sigma) \cdot T_{sk}(\sigma) \end{array}\right\}, \sigma = 1,\cdots, L \quad (4)$$

Hard decoding of $T'_{rk}(\sigma)$ and $T'_{sk}(\sigma)$ yield decisions $I_k(\sigma)$ and $Q_k(\sigma)$, which are then used by the phase estimator (for each time offset) as follows:

$$\left.\begin{array}{l} R_{sum}(\sigma) = \sum_N I_k(\sigma)T'_{rk}(\sigma) + Q_k(\sigma)T'_{sk}(\sigma) \\ S_{sum}(\sigma) = \sum_N I_k(\sigma)T'_{sk}(\sigma) - Q_k(\sigma)T'_{rk}(\sigma) \\ \theta(\sigma) = 0.5\tan^{-1}\left[S_{sum}(\sigma)/R_{sum}(\sigma)\right] \end{array}\right\}, \sigma = 1,\cdots, L \quad (5)$$

The 8-PSK PTCM decoder inputs are quantized phase (ambiguous to 180°) rotated decision variables.

For Gaussian noise and equi-probable 16-QAM, phase (ambiguous to $n\cdot\pi/2$, n=1,2,3) is calculated from any one channel's (e.g., Q) 4th moment to squared variance ratio[3]:

$$\phi = \frac{\pi}{8} - \frac{1}{4}\cdot\sin^{-1}\left[\frac{1}{b}\cdot\left(a\left\{1 + \frac{1}{3.667}\cdot\frac{N}{S}\right\} - \frac{E\left[Q^4\right]}{E\left[Q^2\right]^2}\right)\right] \quad (6)$$

Since $E_s/N_0 > 14$dB for 16-QAM, signal-to-noise ratio estimation in (6) may be omitted. a and b, 1.98 and 0.34 respectively for unshaped 16-QAM, weakly depend on pulse-shaping. Near $\phi = \pi/8$, the arcsin function may be omitted, yielding Figure 5's 16-QAM DPLL structure. AGC-based pre-scaling (shown in Figure 4) aids fixed-point calculation of $E[Q^4]/E^2[Q^2]$. The Viterbi decoder resolves ±90° ambiguity, while the unique-word based R-S frame synchronizer resolves 180° ambiguity.

---

[2]The signs of y and x select an unambiguous quadrant of $\tan^{-1}$ (y/x).

[3]Determining the hard decoding signal set to realize a DDPLL for a non-linearly amplified 16-QAM increases computational requirements.
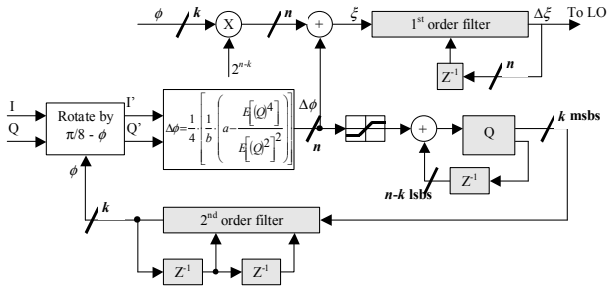
Figure 5. Kurtosis-based 16-QAM digital PLL (modules common to MPSK DDPLL are shaded); $n>k$

QPSK, 8-PSK and 16-QAM soft decisions are $T_{rk}(\sigma_m)$ and $T_{sk}(\sigma_m)$, BPSK using just $T_{rk}(\sigma_m)+T_{sk}(\sigma_m)$. E_b/N_0 vs. BER for QPSK, 8-PSK (TCM metrics set in [8]) and 16-QAM (PLL phase noise included) are shown in Figure 6.
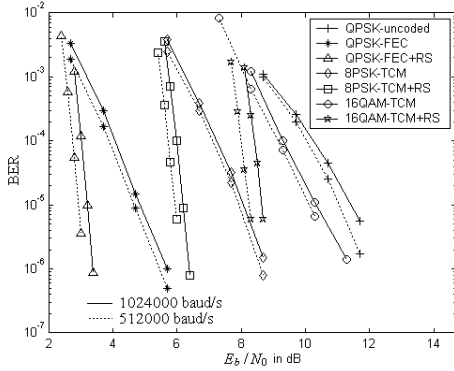
Figure 6. QPSK/ 8-PSK/16-QAM BER performance

During burst-mode frequency and phase[4] acquisition, the BPSK/ QPSK DDPLL yields an unambiguous carrier phase with respect to each assumed baud time hypothesis. Using the QPSK DDPLL for 8-PSK burst-mode[5] acquisition circumvents the 8-PSK phase estimator's inherent 180° phase ambiguity, thereby yielding a frequency tracking range $f_t=k_1/(4\cdot T_s\cdot M\cdot N)$ Hz (k_1^{-1}=phase tracking time constant) for MPSK. Similarly, the QPSK DDPLL is also used for 16-QAM burst-mode acquisition.

4. CARRIER ACQUISITION

For continuous mode MPSK, carrier acquisition removes modulation (exponentiating[6] the signal, and thereby reducing in-band S/N, by M), while for burst-mode, an un-modulated preamble field is exploited for quick acquisition. In both cases, the receiver applies a

Chebyshev window[7] and calculates DFT[8] envelopes, y_1 and y_2, at two equidistant bins from the nominal carrier. Averaging periodograms over K (4 for burst mode and 1024 for continuous mode) 50% overlapped segments improves SNR by almost K. The frequency offset, Δf, is obtained as a function of y_2/y_1[9] (shown in Figure 7 for burst-mode), where f_{bin} is the optimum DFT bins' position (minimizing the probability that frequency offset error, over a desired acquisition range and SNR, exceeds the PLL's frequency tracking range) from the nominal carrier, normalized to the DFT window duration's reciprocal.
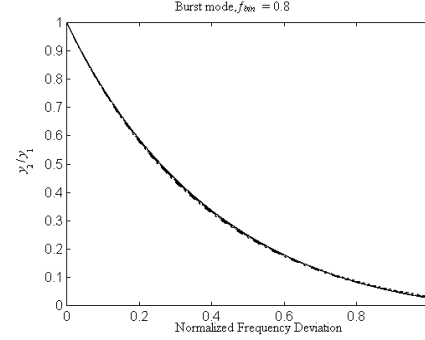
Figure 7. Relation between frequency offset and y_2/y_1

The continuous mode functional relationship depends, due to pulseshaping- and ISI- induced spectral envelope fluctuations, upon modulation type, window length and baud-rate as shown by Table 2 and Figure 8.

Operating Mode	Baud rate (symbols/sec)	Window duration (µs)		Side-lobe (attn. dB)	
		Coarse acq.	Fine acq.	Coarse acq.	Fine acq.
Burst-mode	1024k	15.625	-	40	-
	512 k	31.25	-	44	-
	256 k	62.5	-	46	-
	128 k	125	-	48	-
Continuous mode BPSK	1024k	5.2	10.4	33	40
	512 k	10.4	20.8	40	43
	256 k	20.8	41.6	43	44
	128 k	41.6	83.2	44	45
Continuous mode QPSK	1024k	5.2	10.4	38	45
	512 k	10.4	20.8	45	52
	256 k	20.8	41.6	52	54
	128 k	41.6	83.2	54	57
Continuous mode 8-PSK	1024k	5.2	10.4	27	40
	512 k	10.4	20.8	40	53
	256 k	20.8	41.6	53	54
	128 k	41.6	83.2	54	59
Continuous mode 16-QAM	1024k	10.4	20.8	40	52
	512 k	20.8	41.6	43	57
	256 k	41.6	83.2	41	58
	128 k	83.2	166.4	44	62

Table 2. Chebyshev acquisition windows

---

[4]Absolute encoding provides improved burst-mode BER performance with only slightly increased burst loss probability due to cycle slips.

[5]Continuous-mode decoding (inverting Figure 2's ambiguity encoder) recovers data for $k\pi/8$, $k=0,\dots,7$, initial phase offsets or cycle-slips.

[6]By 16 for 16-QAM, since its phases are approximately a subset of 12 of 16 equally-spaced phases. This approximation, as well as amplitude modulation, results in a less localized spectral peak after exponentiation, which Figure 8's 16-QAM offset curves take into account.

[7]Chebyshev windows [9], with $1.5\leq\alpha\leq3$, suppress out-of-band noise and interference by 30-60dB, while incurring processing losses of 3-3.23dB.

[8] DFT-based acquisition is robust in many noise/ interference scenarios.

[9]This estimator enables an acquisition procedure which decreases the offset progressively and rapidly; in contrast, a PLL's phase estimates become uncorrelated once the offset exceeds its limited tracking range.
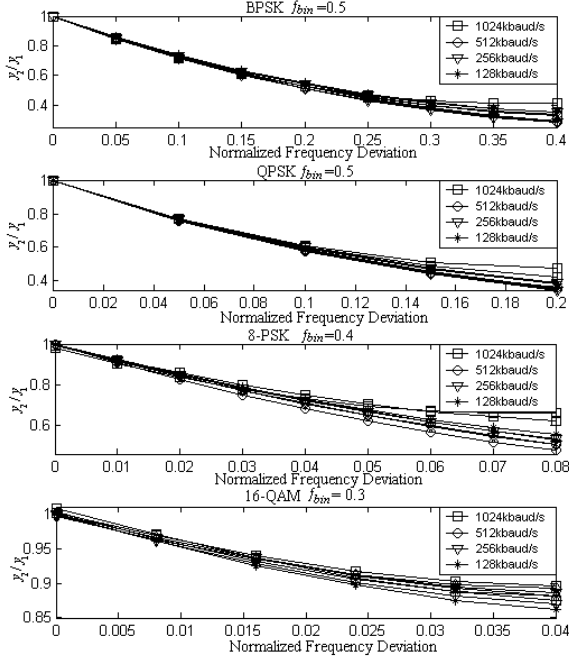
Figure 8. Relationship between offset and y_2/y_1 for the continuous modes of Table 2

The burst loss probability, at offset f_0 and $M(\cdot)$ mapping Δf to r, is:

$$p\left(\left|f_0 - \hat{f}_0\right| > f_t\right) = 1 - \int_{M(f_0-f_t)}^{M(f_0+f_t)} f_{\hat{r}}(\hat{r}/f_0)\, d\hat{r} \qquad (7)$$

The pdf of the ratio, $\hat{r} = \hat{y}_1/\hat{y}_2$, has upper-bound:

$$f_{\hat{r}}(\hat{r}/\Delta f) \le \sqrt{\frac{\hat{r}}{y_1 y_2}} \cdot \frac{1}{2\pi\sigma^2} \int \hat{y}_2^2 \cdot e^{\frac{-\left[(\hat{r}\hat{y}_2 - y_1)^2 + (\hat{y}_2 - y_2)^2\right]}{2\sigma^2}}\, d\hat{y}_2, \quad \text{for}$$

$\dfrac{y_1 \cdot \hat{y}_1}{\sigma^2} \gg 1$, $\dfrac{y_2 \cdot \hat{y}_2}{\sigma^2} \gg 1$, where $\hat{y}_1$, $\hat{y}_2$ are estimated DFT envelopes. Figures 9 and 10 show upper bounds on single-iteration lock failure probabilities for 8-PSK continuous and MPSK burst modes.
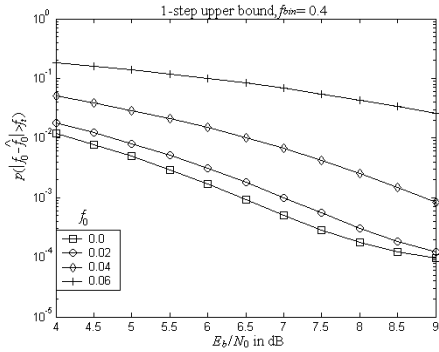
Figure 9. Single-iteration 8-PSK/ PTCM continuous mode lock failure probabilities as functions of normalized (to 96kHz) frequency offsets, with f_t=0.0167.
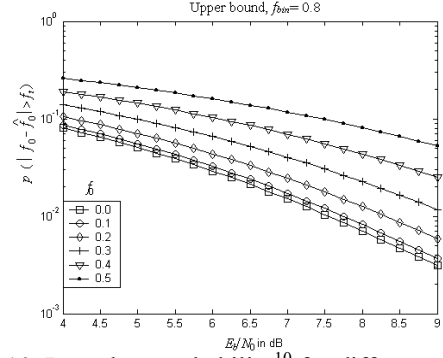
Figure 10. Burst loss probability[10] for different normalized (to 64kHz) frequency offsets. f_t=0.125.

The look-up table-based frequency offset estimator has poor discrimination at small offsets[11] (normalized to the reciprocal of window duration) and high noise susceptibility at large offsets. In continuous mode, using short windows initially (for large offsets) and progressively longer windows as the offset reduces allows frequency acquisition for both small and large offsets. The longest window used decides the error probability, as the iterative algorithm eventually drives (by tuning a NCO) to lower offsets. Moreover, even with a fixed window length, the probability of acquisition improves at lower offsets, as illustrated by the pdfs of the ratio $\hat{y}_2 / \hat{y}_1$ in Figure 11.
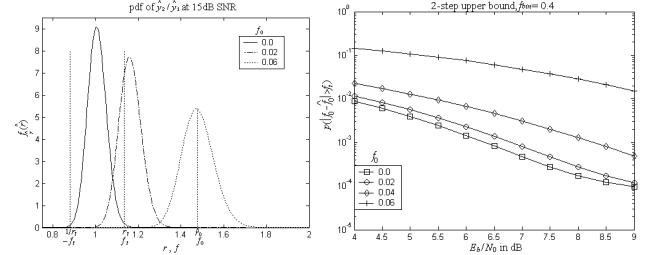
Figure 11. Reduced variance pdfs at lower offsets allow iterated acquisition in continuous mode

5. CONCLUSION

Re-usable and re-configurable modules that realize multi-mode modems, e.g., in an SDR framework [10], overcomes memory/ DSP processing power (or FPGA gate-count/ speed) limitations, without compromising performance. We show that:

- Pulse-shaping components used for HOM, i.e., 16-QAM, may be reused for lower order CEMs
- QPSK demodulation modules may be reused for all CEMs and 16-QAM
- A common module may acquire CEM/ 16-QAM carrier.

---

[10] Network-specific burst acquisition performance is further enhanced, e.g., in a TDMA network, when a receiver initializes its LO using a table of slot frequency offset estimates (that is updated after each successfully received burst), while limiting LO correction during acquisition.

[11] In contrast, the DDPLL excels at tracking small offsets.

APPENDIX 1

With m=3 symbols decision window the power spectrum of the pulse-shaped signal is:

$$S(f) = \frac{1}{T_s} \sum_{j=0}^{4^m-1} \pi_j \left| s_j(f) \right|^2 + \frac{2}{T_s} \sum_{j=0}^{4^m-1} \sum_{k=0}^{4^m-1} \pi_j s_j^*(f) s_k(f) Q_{jk}(f)$$, where $s_j(f)$

is the jth pulse's Fourier transform, π_j the jth state's stationary probability (i.e., 1/64), $Q_{jk}(f) = \sum_{n=1}^{\infty} p_{jk}^{(n)} e^{-j2\pi f nTs}$

the j-to-k state transition probability generating function, derived from $p_{jk}^{(n)}$, the j-to-k n-step transition probability.

$$Q_{10} = \frac{1}{64} e^{-j6\pi fT_s} + \frac{1}{64} e^{-j8\pi fT_s} + \cdots = \frac{1}{64} \cdot \frac{e^{-j6\pi fT_s}}{1 - e^{-j2\pi fT_s}}$$

$$Q_{04} = \frac{1}{16} e^{-j4\pi fT_s} + \frac{1}{64} e^{-j6\pi fT_s} + \cdots = \frac{1}{16} \cdot e^{-j4\pi fT_s} + Q_{10}$$

$$Q_{00} = \frac{1}{4} e^{-j2\pi fT_s} + \frac{1}{16} e^{-j4\pi fT_s} + \frac{1}{64} e^{-j6\pi fT_s} + \cdots = \frac{1}{4} \cdot e^{-j2\pi fT_s} + Q_{04}$$

$$Q_{14} = \frac{1}{4} e^{-j2\pi fT_s} + 0 + \frac{1}{64} e^{-j6\pi fT_s} + \cdots = \frac{1}{4} \cdot e^{-j2\pi fT_s} + Q_{10}$$

For Table 1's pulse-shapes, the generating functions are:

$$B = \begin{bmatrix} Q_{00} & Q_{04} & Q_{04} & Q_{04} & Q_{10} & Q_{10} & Q_{10} & Q_{10} \\ Q_{10} & Q_{14} & Q_{10} & Q_{10} & Q_{04} & Q_{04} & Q_{04} & Q_{04} \\ Q_{10} & Q_{10} & Q_{14} & Q_{10} & Q_{10} & Q_{10} & Q_{10} & Q_{10} \\ Q_{10} & Q_{10} & Q_{10} & Q_{14} & Q_{10} & Q_{10} & Q_{10} & Q_{10} \\ Q_{04} & Q_{04} & Q_{04} & Q_{04} & Q_{14} & Q_{10} & Q_{10} & Q_{10} \\ Q_{10} & Q_{10} & Q_{10} & Q_{10} & Q_{04} & Q_{14} & Q_{04} & Q_{04} \\ Q_{10} & Q_{10} & Q_{10} & Q_{10} & Q_{10} & Q_{10} & Q_{14} & Q_{10} \\ Q_{10} & Q_{10} & Q_{10} & Q_{10} & Q_{10} & Q_{10} & Q_{10} & Q_{14} \\ Q_{04} & Q_{04} & Q_{04} & Q_{04} & Q_{10} & Q_{10} & Q_{10} & Q_{10} \\ Q_{10} & Q_{10} & Q_{10} & Q_{10} & Q_{04} & Q_{04} & Q_{04} & Q_{04} \\ Q_{10} & Q_{10} & Q_{10} & Q_{10} & Q_{10} & Q_{10} & Q_{10} & Q_{10} \\ Q_{10} & Q_{10} & Q_{10} & Q_{10} & Q_{10} & Q_{10} & Q_{10} & Q_{10} \\ Q_{04} & Q_{04} & Q_{04} & Q_{04} & Q_{10} & Q_{10} & Q_{10} & Q_{10} \\ Q_{10} & Q_{10} & Q_{10} & Q_{10} & Q_{04} & Q_{04} & Q_{04} & Q_{04} \\ Q_{10} & Q_{10} & Q_{10} & Q_{10} & Q_{10} & Q_{10} & Q_{10} & Q_{10} \\ Q_{10} & Q_{10} & Q_{10} & Q_{10} & Q_{10} & Q_{10} & Q_{10} & Q_{10} \end{bmatrix}$$

The generator matrix $Q = \begin{bmatrix} B & FB \\ B & FB \\ B & FB \\ B & FB \end{bmatrix}$,

where FB is the matrix obtained by flipping B first left-right and then up-down. Interpolating the 2-sample waveforms (in Table 1) by periodic replication and using an up-sampling filter, the spectrum of each pulse is obtained as:

$$s_j(f) = \frac{1}{N} \sum_{n=-(N-1)/2}^{(N-1)/2} s_j(n) \cdot \exp\left(\frac{-j2\pi f n}{N}\right)$$

The pulse-shaped 8-PSK power-spectrum, obtained using interpolated pulses, with 5.35dB suppression at 0.167 of the uncoded bit rate, is shown in Figure 12. A surface acoustic wave filter further suppresses modulator side-lobes in order to meet the IESS-310 [11] spectral mask[12].

---

[12] An equal symbol-rate unequally-spaced (with phase error at intermediate amplitude being ≈4° from ideal) 16-QAM constructed using I, Q=±a and ±b (the same levels as 8-PSK), with identical pulse-shaping, has identical spectrum (as the I/Q NRZ transitions remain uncorrelated and there being no change to the transition probabilities $p_{jk}^{(n)}$).
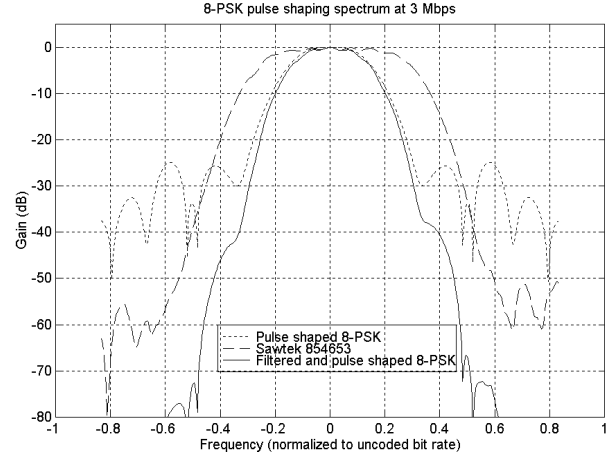
Figure 12. 8-PSK pulse-shaped spectrum

REFERENCES

[1] J.H. Reed, *Software Radio: A Modern Approach to Radio Engineering*, Prentice Hall, NJ, 2002, pp. 2-8.

[2] EN 301 210 *Digital Video Broadcasting* (DVB); Framing structure, channel coding and modulation for *Digital Satellite News Gathering* (DSNG) and other contribution applications by satellite, v1.1.1 (1999-03).

[3] K. Feher, *Wireless Digital Communications*, Prentice Hall, 1995, pp. 117-133.

[4] S. Jayasimha and P.K. Singh, "Design of Nyquist and near Nyquist pulses with spectral constraints," *Proceedings of ICPWC-2000*, pp. 38-42.

[5] Y. Neuvo, C-Y. Dong and S.K. Mitra, "Interpolated finite impulse response filters," *IEEE Transactions on Acoust. Speech and Signal Processing* vol. ASSP-32, pp. 563-570, June 1984.

[6] M.P. Fitz and J-M. Cramer, "A performance analysis of a Digital PLL based MPSK demodulator," *IEEE Transactions on Communications*, vol. 43, no. 2/3/4, February/March/April 1995, pp. 1192-1201.

[7] C.G. Hiremath and S. Jayasimha, "Design of burst mode decision-feedback QPSK demodulator," *Proceedings of SPCOM-1999*, pp. 133-139.

[8] S. Jayasimha and P. Jyothendar, "Pragmatic TCM for 8-PSK in Satellite Communications," *Proceedings of SPCOM-2001*, pp. 129-134.

[9] F.J. Harris, "On the use of windows for harmonic analysis with the Discrete Fourier Transform," *Proceedings of the IEEE*, vol. 66, no. 1, January 1978, pp. 51-83.

[10] L. Pucker and G. Holt, "Extending the SCA core framework inside the modem architecture of a software defined radio," *IEEE communications*, vol. 42, no. 3, March 2004, pp. S21-S25.

[11] *Intelsat Earth Station Standards* (IESS), Document IESS-310 (Rev. 3), January 31, 2003.